Dalton Transactions

PAPER

View Article Online
View Journal | View Issue

Cite this: *Dalton Trans.*, 2026, **55**, 1697

Published on 22 December 2025. Downloaded on 4/26/2026 2:36:15 AM.

Amino-modified halloysite nanotube-supported nickel catalysts for the efficient reductive amination of biomass aldehydes and ketones

Weihong Li,[a] Nan Zhong,[b] Yifei Yin,[b] Weiming Xiao,[a] Shunmin Ding,[a] Rongping Zhou,[c] Chao Chen[a] and Shengjun Deng *[a]

Received 12th November 2025, Accepted 19th December 2025

DOI: 10.1039/d5dt02705e

rsc.li/dalton

The reductive amination of biomass aldehydes and ketones to synthesize primary amines is a highly promising strategy for the conversion of biomass into value-added products. In this study, non-precious metal Ni was loaded onto halloysite nanotubes (HNTs) modified by gamma aminopropyltriethoxysilane (APTES) using an impregnation-chemical reduction method to prepare a series of efficient nickel-based catalysts (denoted as Ni-WHNT) with different Ni loadings. The compositions and structures of the prepared catalysts were characterized by XPS, TEM, SEM, and so on. The Ni-WHNT catalyst with 10 wt% Ni facilitated the efficient synthesis of furfurylamine (FAM) in the reductive amination of biomass furfural (FAL) and displayed a FAM yield of 99% under mild conditions (90 °C, 0.5 MPa H_2, and 0.3 MPa NH_3). Moreover, the catalyst exhibited a broad scope of various other aldehyde and ketone substrates and could be recycled up to 5 times without any significant loss of activity. Additionally, the catalytic mechanism and structure–activity relationship were investigated.

Introduction

The tandem reductive amination of biomass aldehydes/ketones is of great significance, which not only reduces dependence on fossil fuels and lowers carbon footprint on the Earth but also sustainably produces useful primary amines.[1] Additionally, the primary amines can be used as key building units in pharmaceuticals, agricultural chemicals, polyamides, and other fine chemicals.[2] It is well known that the biomass aldehydes/ketones can be easily obtained from lignocellulosic biomass.[3,4] Compared to other methods such as hydrogenation amination of olefins,[5] amination of aryl halides,[6] and reduction of specific nitrogen sources (oximes,[7] nitriles,[8] and nitro compounds[9–13]) used for the synthesis of primary amines, the catalytic reductive amination of carbonyl compounds using NH_3 as the nitrogen source and H_2 as the reducing agent has become the preferred solution for industrial and academic research due to its simple operation and high efficiency.[14–17] To date, various metal catalysts have been explored for the reductive amination of carbonyl compounds.[18] However, this process faces the following challenges: primary amines are prone to over amination or over hydrogenation to alcohols on highly active precious metals (such as Pd and Pt), and trimer by-products are easily generated in low-activity catalytic systems, resulting in a lower selectivity.[19,20] Therefore, the design of efficient catalysts for this reaction is attractive and promising. To date, different catalysts have been investigated by optimizing the metal oxidation state, support structure, electron density, support acidity, and so on.[20,21] Among them, non-precious Ni-based catalysts are highly desirable and intensively investigated owing to their superior activity and selectivity. In a study by Sun *et al.*,[22] a Ni_2P@C catalyst has been demonstrated to effectively adjust the particle size, expose specific crystal planes, modulate the electronic properties, and optimize the surface acidity, thereby significantly enhancing the catalytic performance. Meanwhile, Manzoli *et al.* utilized the magnetic properties of nickel and developed Fe_3O_4@SiO_2-Ni catalysts for the reductive amination of carbonyl compounds into primary amines under microwave irradiation. These catalysts exhibit good to excellent activity across a variety of aldehyde substrates, highlighting their versatility and efficiency in facilitating reductive amination reactions.[23] Although extensive literature exists on the use of Ni-based catalysts for the reductive amination of carbonyl compounds, it can be found that most of these catalysts usually require harsh reaction conditions, *e.g.*, high pressure (≥4 MPa) or high temperature.[24] Besides, the preparation of support is cumbersome, which greatly increases the cost of catalysts.

---

[a] *Key Laboratory of Jiangxi Province for Environment and Energy Catalysis, College of Chemistry, Nanchang University, Nanchang, Jiangxi 330031, P.R. China. E-mail: shjdeng@ncu.edu.cn*

[b] *School of Pharmacy, Nanchang University, Nanchang, Jiangxi 330031, P.R. China*

[c] *The first affiliated hospital of Nanchang university, Jiangxi 330006, P.R. China*

Published on 22 December 2025. Downloaded on 4/26/2026 2:36:15 AM.

Therefore, it is highly desirable to develop efficient inexpensive Ni-based catalysts for the reduction amination of carbonyl compounds (aldehydes or ketones) under mild conditions.

It is known that the support of the metal catalyst plays a crucial role in determining the catalytic performance, and the selection of a suitable support is one of the key factors for the supported catalyst. Halloysite nanotubes (HNTs), natural mineral materials, provide an ideal platform for the construction of supported catalysts:[25,26] (1) their natural hollow tubular structure endows them with high specific surface area and abundant pores, which are conducive to the mass and heat transfer;[27] (2) the chemical heterogeneity of the inner and outer surfaces (with the outer surface being siloxane (Si–O–Si) and the inner surface being rich in aluminum hydroxyl groups (Al–OH)) provides unique possibilities for physical modification;[28,29] (3) excellent chemical and thermal stabilities ensure that the catalyst maintains structural integrity under reducing amination conditions; (4) benefiting from the natural abundance and low cost of halloysite, the catalytic system has significant economic advantages; (5) the main constituent elements of HNTs are Al, Si, and O, and many previous works have indicated that the surface Lewis site Al^{3+} is responsible for the adsorption of N-containing intermediates;[30,31] and (6) the surface of the HNT contains abundant hydroxyl groups, making it easy to undergo surface modification. We found that the gamma aminopropyltriethoxysilane (APTES) bearing an amino group ($-NH_2$) can provide an alkaline microenvironment, optimize the amination process, improve the yield of primary amines, and lower the reaction temperature.[32] Moreover, APTES can form stable covalent bonds with the hydroxyl groups on the surface of HNTs, significantly improving metal dispersion by enhancing the metal support interaction, thereby enhancing the catalytic stability.[33–36] However, as a potential catalyst support candidate, the HNT has not yet been used for the reductive amination reaction to date.

Considering the acidity and unique structure of the HNT, the basicity and adhesion of APTES, and the hydrogenation capability of nickel, we herein designed and prepared a novel catalytic system (Ni-WHNT) using APTES-modified HNT-supported nickel. In addition, the catalytic system was applied to the reductive amination of biomass-based furfural (FAL) to furfurylamine (FAM) (Scheme 1) for the first time. As expected, the integration of HNTs and APTES as well as nickel does create a synergistic catalytic effect. Consequently, 10 wt% Ni-loaded WHNT exhibited excellent performance in the reductive amination of FAL: achieving a 99% yield of FAM under mild conditions (90 °C, 0.5 MPa H_2, and 0.3 MPa NH_3) and demonstrating excellent universality (81–99% yield of primary amines) and stability for various aldehyde ketone substrates. Moreover, the results revealed that the APTES-modified HNT was an excellent support. Furthermore, a comprehensive investigation into the structure–activity relationship and reaction mechanism was conducted to elucidate the origins of high performance.

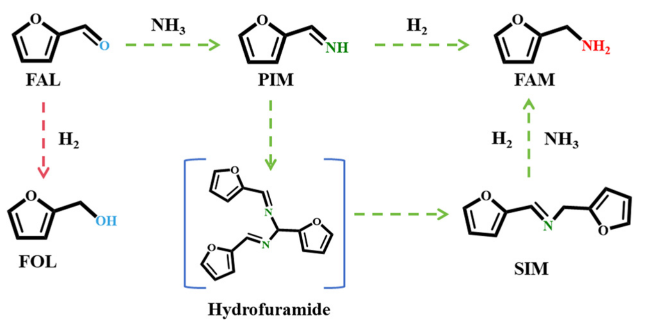

Scheme 1 Reaction pathway for the conversion of FAL to FAM.

Experimental

Materials and characterization instruments

Detailed information on the chemicals and characterization instruments used is given in the Experimental details section of the SI.

Catalyst preparation

First, APTES was used to modify HNTs. The typical preparation steps are as follows: 2 g of HNT was dispersed in 50 mL of deionized water, and 0.06 g of $NaHCO_3$ was added, stirred and refluxed at 80 °C for 2 h. Then, the pH of the reaction solution was adjusted to 8–9 with sulfuric acid, and 1 mL of APTES was added with continuous stirring followed by refluxing at 80 °C for 4 h. Finally, the obtained precipitate was separated by filtration, washed three times with deionized water and then vacuum freeze-dried to obtain APTES-functionalized HNTs (WHNTs).

Ni-WHNTs with different nickel loadings were prepared by an impregnation-chemical reduction method. Typically, the WHNT and $Ni(NO_3)_2 \cdot 6H_2O$ with an adjustable WHNT : Ni mass ratio were added to 40 mL of deionized water. The reaction mixture was stirred for 1.5 h and then stirred for another 0.5 h in an ice water bath. Afterwards, a freshly prepared ice aqueous solution of sodium borohydride ($NaBH_4$ is 5 equiv. to Ni) was added into the above mixture and then stirred for 1 h. The precipitate was obtained by filtration, washed three times with deionized water, and then washed once with ethanol. After vacuum drying, Ni-WHNTs with different nickel loadings were obtained. Ni/Al_2O_3 and Ni/SiO_2 catalysts were also prepared by the similar methods.

Catalytic measurements

Typically, 1 mmol of FAL, 0.05 g of catalyst, and 15 mL of isopropanol were added and mixed in a 100 mL stainless-steel high-pressure reactor. After sealing, the reactor was rinsed 7–10 times with H_2 (99.999%). After 0.5–1.0 MPa H_2 and 0.2–0.4 MPa NH_3 were filled, the experiments were conducted at the desired temperature (90–120 °C) and a specified reaction time (3–6 h) under constant magnetic stirring (450 rpm). The extracted reaction mixture was determined by gas chromatography-mass spectrometry (GC-MS) using a GC-MS

This journal is © The Royal Society of Chemistry 2026

Published on 22 December 2025. Downloaded on 4/26/2026 2:36:15 AM.

7890B-5977A with an Agilent 19091S-433 capillary column (HP-5MS, 30 m × 250 μm × 0.25 μm). After the reaction was over, the used catalyst was washed with ethanol and dried for the next cycle of experiment. For the accuracy, all experiments were repeated three times, and the average values were taken with the analysis error not more than 5%.

Results and discussion

Composition and structure of catalysts

The HNT was functionalized with APTES to introduce the amino groups. The Ni nanoparticles (NPs) were produced directly on the surface *via in situ* reduction of $Ni(NO_3)_2$ by sodium borohydride (Fig. S1), thereby producing the Ni-WHNT catalysts.

Ni-WHNTs with different nickel loadings were prepared by an impregnation-chemical reduction method. The Ni content of the Ni-WHNT samples was determined by ICP-OES. The contents of Ni on 5%Ni-WHNT, 10%Ni-WHNT, and 15%Ni-WHNT were 4.63%, 9.33%, and 13.89%, respectively. The Ni content on 10%Ni-HNT was found to be 9.04%, which was lower than that on 10%Ni-WHNT (9.33 wt%) (Table S1). This result showed that the amino group on WHNT was conducive to graft more Ni NPs.

The XRD patterns of samples are shown in Fig. 1a. HNT, WHNT, and Ni-WHNT all exhibit diffraction peaks at 2θ = 11.79°, 20.07°, 24.50°, 35.02°, 54.65°, and 62.67°, corresponding to the (001), (100), (002), (110), (210), and (300) crystal planes, respectively, which are consistent with the diffraction peaks of HNT's PDF card.[37] This indicates that the original structure of HNT is still maintained after APTES modification and Ni loading. Compared to the original HNT, the characteristic peak of Ni was not observed in all Ni-WHNT catalysts, resulting from the smaller size and high dispersion of the Ni NPs.[38]

Fig. 1b shows the FT-IR spectra of the samples. The absorption bands at 3622 cm^{-1} and 3700 cm^{-1} correspond to the stretching vibration of the hydroxyl groups of the inner surface of the HNT. The absorption bands near 3448 cm^{-1} and 1625 cm^{-1} are related to the stretching and bending vibrations of the hydroxyl groups from the adsorbed water on the surface of the HNT, respectively. While the peak at 916 cm^{-1} corresponds to the bending vibration of the hydroxyl groups (Al–OH), the in-plane stretching vibration band of the Si–O appears at 1025 cm^{-1} in the silicate layers. Meanwhile, the in-phase stretching band of the apical Si–O bonds appears near 1080 cm^{-1}. The perpendicular vibration bands of Si–O appear at 745 cm^{-1} and 685 cm^{-1}. The absorption bands at 530 cm^{-1} and 465 cm^{-1} are caused by the bending vibration of Al–O–Si and Si–O–Si, respectively.[39,40] After APTES modification, the peak positions and intensities of Si–O, Al–O–Si, and Si–O–Si in the WHNT and Ni-WHNT samples are similar to those of pristine HNT, indicating that the APTES modification did not damage the silicate structure of the HNT. Meanwhile, several new peaks can be found for WHNT and Ni-WHNT compared with the pristine HNT. The absorption bands at 2910 cm^{-1} and 1310 cm^{-1} are related to the symmetric stretching and deformation $-CH_2$ vibration, respectively. In addition, the peak at 1480 cm^{-1} is attributed to the deformation vibration of N–H. The results confirm that APTES was successfully loaded onto the HNT surface. However, it is worth noting that the characteristic absorption strengths of the water OH stretching vibration (*ca.* 3448 cm^{-1}) and the deformation (*ca.* 1625 cm^{-1}) remain almost unchanged before and after modification. This demonstrates that only a small part of –OH on the HNT surface is involved in the silanization reaction.[5]

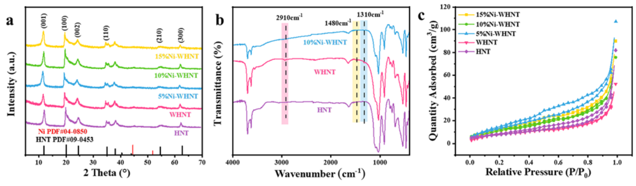

Fig. 1 (a) XRD patterns, (b) FT-IR spectra, and (c) N_2 adsorption–desorption isotherms of the HNT, WHNT, and Ni-WHNT.

Fig. 1c shows the nitrogen adsorption/desorption curves of samples. Obviously, all catalysts belong to the type IV adsorption isotherms, implying that they are typical mesoporous materials. Table 1 lists the BET specific surface areas and average pore diameters of the catalysts. It can be observed that the average pore diameters of the HNT decrease after modification. This indicates that grafting primarily occurs between hydrolyzed APTES and surface hydroxyl groups, and partial grafting may occur on the aluminum-alcohol groups on the inner surface of the lumen, as well as on aluminum-alcohol and silicon-alcohol groups at defects on the edges or outer surface.[5] For the BET, there was no significant change after APTES modification, while the specific surface areas of the catalysts slightly increased after Ni loading, indicating the successful introduction of Ni NPs into the WHNT. There is a slight increase in surface area because the Ni NPs loaded on the HNT are relatively small and mostly on the outer surface, which can be confirmed by the subsequent EDS.

The SEM images of the samples are shown in Fig. 2. From Fig. 2a and b, it can be seen that both the modified and unmodified HNTs maintain a tubular structure, indicating that the modification does not affect their morphology. Besides, from Fig. 2c–f, it can also be observed that the Ni NPs on the surface of the HNT modified with APTES (10%Ni-WHNT) are denser and more uniform than the unmodified HNT-sup-

Table 1 BET surface area and average pore size of the samples

Entry	Catalysts	S_{BET} (m^2 g^{-1})	Average pore size (nm)
1	HNT	28	18.09
2	WHNT	30	10.78
3	5%Ni-WHNT	55	12.17
4	10%Ni-WHNT	46	10.11
5	15%Ni-WHNT	44	12.77

Published on 22 December 2025. Downloaded on 4/26/2026 2:36:15 AM.

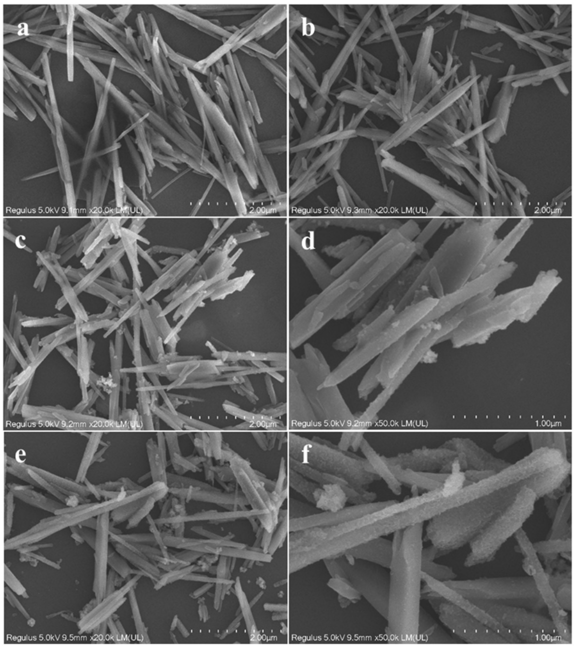

Fig. 2 SEM images of (a) HNT, (b) WHNT, (c and d) 10%Ni-HNT, and (e and f) 10%Ni-WHNT.

ported Ni catalyst (10%Ni-HNT), and there is almost no agglomeration on 10%Ni-WHNT. This result indicates that APTES can improve the distribution of Ni NPs through its branch amino groups.

To further investigate the presence of $-NH_2$ groups and the effect of APTES modification on the state of Ni NPs on the catalyst surface, HNT, 10%Ni-HNT, 2%Ni-WHNT and 10%Ni-WHNT were characterized by the TEM and EDS, and the results are shown in Fig. 3 and Fig. S8. It can be found that both the 10%Ni-HNT and 10%Ni-WHNT catalysts possessed well-defined tubular structures, indicating that the main structure of the HNT was maintained after APTES modification and Ni NP loading, while Ni NPs were observed to exist on both the inner and outer surfaces of the HNT. In contrast to the 10% Ni-HNT catalyst (Fig. 3f–h), Ni NPs on the 10%Ni-WHNT catalyst (Fig. 3a–c) are highly, densely and uniformly distributed, indicating that the $-NH_2$ group can effectively improve the dispersion of metal nanoparticles. The EDS (Fig. 3d and f) further indicated the uniform distribution of Ni and N elements on the surfaces of the APTES-modified HNT support. The HRTEM images of the 10%Ni-WHNT and 10%Ni-HNT catalysts reveal the observed crystal finger spacings of 0.203 nm, which can be indexed to the (111) plane of Ni NPs (Fig. 3e and j). In addition, no obvious XRD characteristic peaks of Ni in 10%Ni-WHNT were detected, which can be attributed to the ultrafine particle size of Ni NPs. Similarly, Ni nanoparticles of 2%Ni-WHNT are also highly dispersed but have a significantly lower particle density.

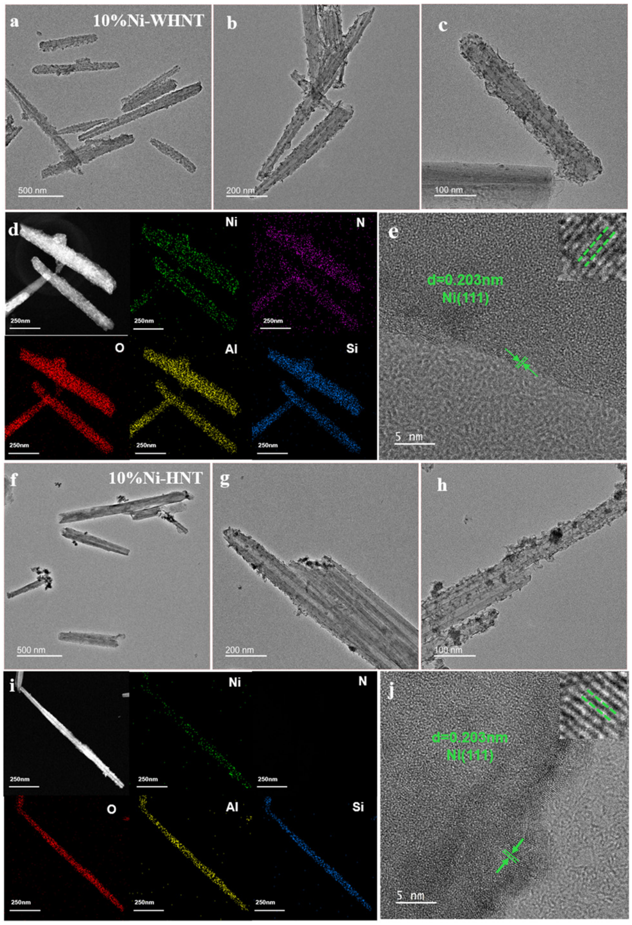

Fig. 3 TEM images of (a–c) 10%Ni-WHNT and (f–h) 10%Ni-HNT. The corresponding EDS mappings of (d) 10%Ni-WHNT and (i) 10%Ni-HNT. HRTEM images of (e) 10%Ni-WHNT (inset: its enlarged image) and (j) 10%Ni-HNT (inset: its enlarged image).

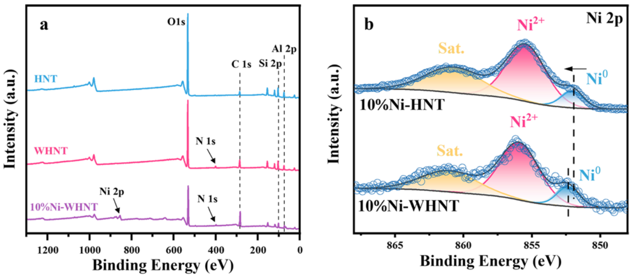

Fig. 4 XPS spectra of (a) total survey and (b) Ni 2p of the HNT, 10%Ni-WHNT and WHNT.

In order to investigate the chemical states of metal elements and the interaction between the metal and the support in the as-prepared catalysts, XPS was used to characterize the samples. As shown in Fig. 4a, the survey XPS spectrum of the HNT shows the characteristic peaks of Si 2p, Al 2p, and O 1s. The C 1s peak was also observed at 284.8 eV, probably originating from the presence of some impurities adsorbed on the HNT surface when exposed to the atmosphere.[41] Compared to the XPS spectrum of the HNT, a distinct N peak could be observed in the spectra of the APTES-modi-

This journal is © The Royal Society of Chemistry 2026

Published on 22 December 2025. Downloaded on 4/26/2026 2:36:15 AM.

fied HNT catalysts (10%Ni-WHNT and WHNT), confirming the successful grafting of APTES onto the HNT surfaces. For the 10%Ni-WHNT catalyst, the Ni 2p spectrum can be divided into three peaks, where the peaks at 851.88 eV and 852.28 eV are attributed to Ni^0, the peaks at 855.48 eV and 855.98 eV are attributed to Ni^{2+}, and the remaining peaks are satellite peaks of Ni.[42,43] In Fig. 4b, it can be observed that most of the Ni species on the catalyst surface were oxidized. This is because during the characterization process, the catalyst was exposed to air to cause partial oxidation of the surface layer.[44,45] It must be pointed out that the as-prepared catalyst was stored under vacuum after synthesis, as it cannot be preserved for a long time without undergoing oxidation. Compared with the 10%Ni-HNT catalyst, the binding energies of $Ni^{2+}$and Ni^0 peaks in the 10%Ni-WHNT catalyst were positively shifted by 0.5 and 0.4 eV, respectively, which was due to the smaller size of Ni NPs and interaction between Ni NPs and amino groups.[38] The electronegativity of N is higher than that of Ni; hence, when there is interaction between them, partial electron migration from Ni to N may occur.[46] Electron transfer can cause the electrons on the metal surface to readjust, typically making the metal particles more stable and giving rise to the higher catalytic performance.[47,48] In addition, early studies have found that electron transfer leads to the reconstruction of the electronic structure on the metal surface, which can regulate the adsorption configuration of the surface of the active center. This is beneficial for the selective generation of FAM from FAL and avoids hydrogenation of furan rings.[47]

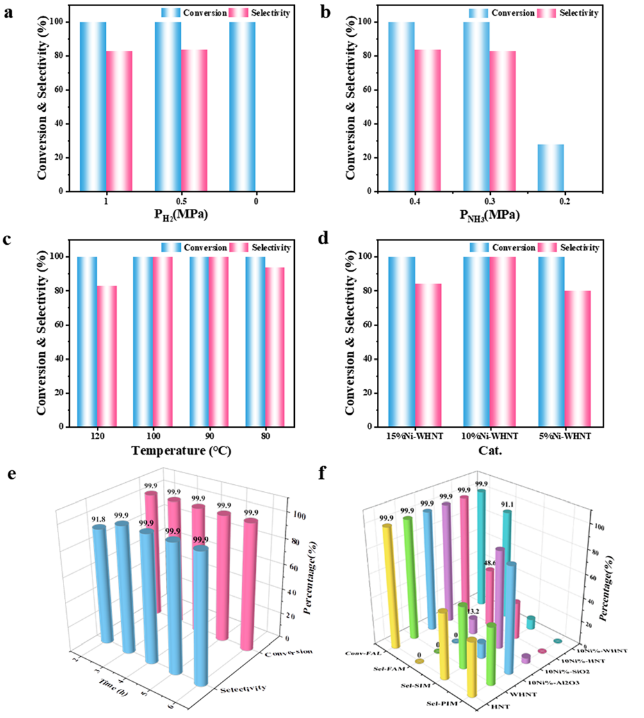

Fig. 5 (a–e) Effects of different hydrogen pressures, ammonia pressures, reaction temperatures, Ni loadings in the catalyst, and reaction times on the FAL conversion rate and FAM selectivity. (f) Comparison of the FAL conversion rate and FAM selectivity over different catalysts.

Catalytic capability

All of these materials were tested in the reductive amination of FAL using ammonia and hydrogen to prepare FAM. The reaction pathway is given in Scheme 1. First, FAL undergoes a condensation reaction with ammonia to generate the corresponding imine (PIM). The PIM is an unstable intermediate and can be converted into SIM by polymerization and hydrogenolysis.[30] SIM reacts with both NH_3 and H_2, and goes through a catalytic hydrogenolysis process to give the desired FAM. Moreover, in the presence of catalyst, PIM can be hydrogenated to produce the desired FAM.[49]

Fig. 5 shows the catalytic activities of the Ni-WHNT catalysts. In Fig. 5a–e, the control variable method was used to optimize the hydrogen pressure, ammonia pressure, reaction temperature, Ni loading in the catalyst, and reaction time. The optimal reaction conditions were obtained as 90 °C, 0.5 MPa H_2, 0.3 MPa NH_3, and 3 h. Under these reaction conditions, the conversion rate and selectivity over the 10%Ni-WHNT catalyst were 99.9% and 99.9%, respectively. It is worth noting that no FAM was generated in the absence of hydrogen, and only intermediates SIM and PIM were obtained (Fig. 5a), indicating that hydrogen is required to generate FAM. When the ammonia pressure was low, FAL could not be completely converted into SIM and PIM, which limited the generation of FAM (Fig. 5b). Afterwards, we investigated the effect of reaction temperature (Fig. 5c) on the catalytic activity. When the temperature was 120 °C, FAL was partially hydrogenated to generate FOL, while when the temperature decreased to 100 °C or 90 °C, FAL was completely converted to the targeted FAM. However, when the temperature was lower, some intermediates were not completely converted. The results indicate that high temperatures can lead to direct hydrogenation of FAL, while low temperatures can weaken the hydrogenation ability, thereby affecting the further conversion of intermediates to FAM. The catalytic performances over Ni-WHNT catalysts with different Ni loadings are shown in Fig. 5d. When the Ni loading increased from 5 wt% to 10 wt%, the conversion rate of FAM increased from 80.3% to 99.9%, respectively. When the Ni loading further increased to 15 wt%, FAL was partially hydrogenated to generate FOL, resulting in a decrease in FAM selectivity. This may be due to the enhanced hydrogenation activity of Ni NPs under high loading conditions, resulting in the direct hydrogenation of FAL. Therefore, the most suitable catalyst in the reductive amination of FAL to FAM should have a moderate but not the highest hydrogenation activity. Finally, the reaction time was screened under the conditions of 90 °C, 0.5 MPa H_2, and 0.3 MPa NH_3 (Fig. 5e). When the reaction time was 2 h, FAL was completely converted and the selectivity of FAM reached 91.8%. When the reaction time was extended to 3 h, FAL was completely converted to FAM, and the catalyst achieved rapid conversion of FAL to FAM under mild conditions.

To further investigate the catalytic performance of modified HNTs, the reaction was also carried out on the HNT, WHNT

Published on 22 December 2025. Downloaded on 4/26/2026 2:36:15 AM.

and 10%Ni-SiO_2 as well as 10%Ni-Al_2O_3 under the obtained optimal reaction conditions, and the results are shown in Fig. 5f. The complete conversion of FAL can be achieved over the HNT, WHNT and 10%Ni-Al_2O_3, but the products are limited to intermediates SIM and PIM. The result indicates that the conversion of intermediate SIM/PIM to targeted FAM depends not only on the activation of H_2 by Ni NPs, but also crucially on the synergistic catalytic effect between Ni species and the support. Over the 10%Ni-SiO_2 and 10%Ni-HNT catalysts, complete conversion of FAL was also achieved, and partial FAM was generated with yields of 13.2% and 48.6%, respectively. This indicates that the introduction of Ni provides the necessary hydrogenation activity, but the nature of the support resulted in a lower efficiency of the intermediate hydrogenation towards FAM. In sharp contrast, the 10%Ni-WHNT catalyst achieved a FAM yield >99% under the same conditions. This performance gap highlights the critical role of APTES modification in optimizing the structure–activity relationship: (1) the $-NH_2$ groups anchor Ni species to form highly dispersed ultrafine nanoparticles (as shown in Fig. 2 and 3), significantly boosting the hydrogenation activity; (2) the introduction of basic sites constructs an acid–base synergistic surface with the HNT, which is essential for high selectivity towards imine condensation; and (3) the strong interaction between N and Ni, as proven by XPS, stabilizes the active phase. In addition, this strong interaction prevents Ni leaching and agglomeration during recycling, thereby significantly enhancing the catalyst stability. Obviously, the APTES-modified WHNT support is superior to the unmodified HNT in simultaneously enhancing the activity, selectivity, and stability.

Under the conditions of 90 °C, 0.5 MPa H_2, 0.3 MPa NH_3, and 3 h of reaction time, the dynamic evolution of substrates and products in the catalytic reaction was investigated (Fig. 6). In the initial stage of the reaction, both intermediates SIM and PIM were detected to be generated simultaneously, followed by rapid and complete conversion of PIM into SIM. At 45 min, FAM began to form, while the concentration of SIM showed a decreasing trend. At the end of the reaction, all SIM intermediates were completely converted into FAM. The gas chromatography analyses clearly revealed the cascade transformation pathway from intermediates to final products. In addition, the inherent surface acidic sites of the HNT exhibit high efficiency in catalyzing the condensation of aldehyde and ammonia to produce imines, thereby accelerating the total amination process. The highly dispersed Ni species on the WHNT surface are responsible for promoting subsequent hydrogenation reactions. Their synergistic effect achieves efficient and direct conversion of FAL to FAM.

To verify the stability of the typical catalyst 10%Ni-WHNT, filtration experiments and cycle tests were conducted separately (Fig. 7a and b). After filtering out the catalyst, there was no significant change in the yield of FAM, indicating that the selective hydrogenation reaction of intermediates (SIM and PIM) to FAM stopped, and the active component (Ni) of the catalyst did not detach. The yield of FAM gradually slows down with the increasing cycle time, but maintains high catalytic activity after the fifth cycle (Fig. 7b). The deactivation of the catalyst in the early stages of cycling is mainly reflected in the decrease of initial reaction rate, rather than a significant decrease in the final yield rate. The initial reaction rate slows down during the early stage of the cycle, which may be attributed to the slight reduction of active Ni^0 site. The ICP-OES analysis showed that the Ni content of the reused 10%Ni-WHNT was 9.25 wt%, which was almost consistent with that (9.33 wt%) of 10%Ni-WHNT before cycling, suggesting that there was basically no loss of Ni. Moreover, there was no significant change in the intensity of diffraction peaks in the XRD patterns of the 10%Ni-WHNT catalyst before and after cycling (Fig. 7c), showing that the structure of the catalyst can be remained. Additionally, the valence state distribution of Ni in the Ni 2p XPS spectra of the 10%Ni-WHNT catalyst before and after cycling was similar (Fig. 7d), indicating that only a small part of the active centers undergoes oxidation or separation, and the overall stability is good.

Obviously, 10%Ni-WHNT exhibited excellent structural and chemical stabilities in multiple cycles of use. By comparing

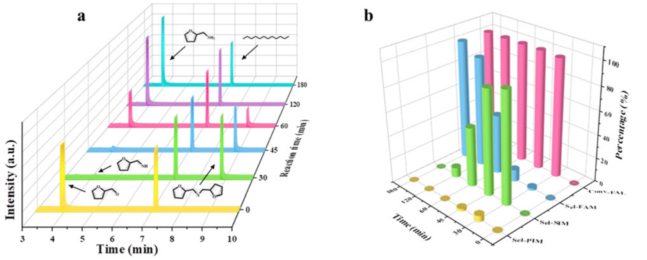

Fig. 6 (a) Gas chromatogram analyses of reaction mixtures over 10%Ni-WHNT as a function of time. (b) Point graph of yield variation over time on 10%Ni-WHNT.

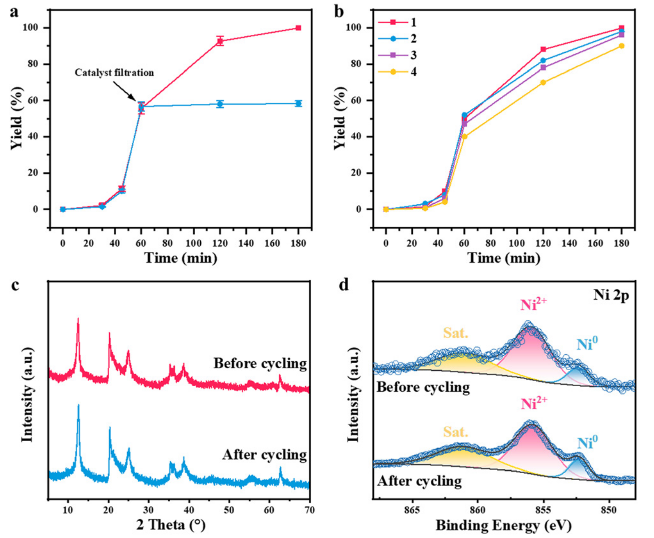

Fig. 7 (a) Filtration experiment for 10%Ni-WHNT. (b) Recycle experiments for 10%Ni-WHNT. (c) XRD patterns of 10%Ni-WHNT before and after cycling. (d) XPS spectra of 10%Ni-WHNT before and after cycling.

Published on 22 December 2025. Downloaded on 4/26/2026 2:36:15 AM.

Table 2 Comparison of the catalytic performance for the reductive amination of FAL to FAM between the reported catalysts and 10%Ni-WHNT

Catalyst	Conditions	Conv. (%)	FAM yield (%)	Ref.
Ru/NC-900-800NH_3	100 °C, 10 h, 2 MPa H_2, 0.5 MPa NH_3	>99	97	63
Ru/TiP-100	30 °C, 24 h, 1.7 MPa H_2, 0.3 MPa NH_3	—	91	64
Ru/γ-Al_2O_3	80 °C, 2 h, 3.0 MPa H_2, 0.4 MPa NH_3	—	75	65
Ru/Nb_2O_5	90 °C, 2 h, 4.0 MPa H_2, 0.4 MPa NH_3	>99	98	20
Co@CoO	90 °C, 4.5 h, 2.0 MPa H_2, 0.4 MPa NH_3	100	98	66
Co@C-N (800)	35 °C, 24 h, 1.7 MPa H_2, 0.3 MPa NH_3	—	70	67
Fe-L2@NC-800	130 °C, 24 h, 4.0 MPa H_2, 0.5 MPa NH_3	>99	85	68
Ni/pNC	60 °C, 6 h, 3.0 MPa H_2, 0.4 MPa NH_3	>99	92	69
Ni/Al_2O_3(111)	60 °C, 4 h, 3.0 MPa H_2, 0.4 MPa NH_3	>99	98	70
Ni/SiO_2-I-DP	90 °C, 1.5 h, 4.0 MPa H_2, 0.8 MPa NH_3	>99	99	71
Ni/MC	80 °C, 12 h, 0.1 MPa H_2, NH_3 (aq.)	>99	88	72
Ni/Al_2O_3	100 °C, 0.5 h, 2.0 MPa H_2, NH_3 (aq.)	>99	99	73
NiAl-10	80 °C, 1 h, 2.0 MPa H_2, 0.5 MPa NH_3	>99	99	74
Ni/α-Al_2O_3	100 °C, 12 h, 2.0 MPa H_2, 0.2 MPa NH_3	>99	95	75
10%Ni-WHNT	90 °C, 3 h, 0.5 MPa H_2, 0.3 MPa NH_3	>99	99	This work

the catalytic performance of Ni-WHNT and other reported catalysts for FAL reduction amination to FAM (Table 2 and Table S4), it can be found that this catalyst is not inferior to precious metal-based catalysts, and the reaction conditions are also relatively mild. Afterwards, the reaction scope of the typical catalyst 10%Ni-WHNT was investigated. Table S2 indicates that the catalyst not only has good universality in gas-phase nitrogen sources, but also has certain universality in liquid-phase nitrogen sources. Moreover, it has good universality in different aldehydes and ketones.

Exploration of the catalytic mechanism

H_2-TPD experiments were conducted to evaluate the hydrogen activation abilities of the HNT, WHNT, and Ni-WHNT. The results indicated that the catalyst loaded with Ni had a lower desorption temperature (Fig. 8a), and with the increase in Ni loading, the catalyst showed a stronger ability to activate hydrogen molecules.

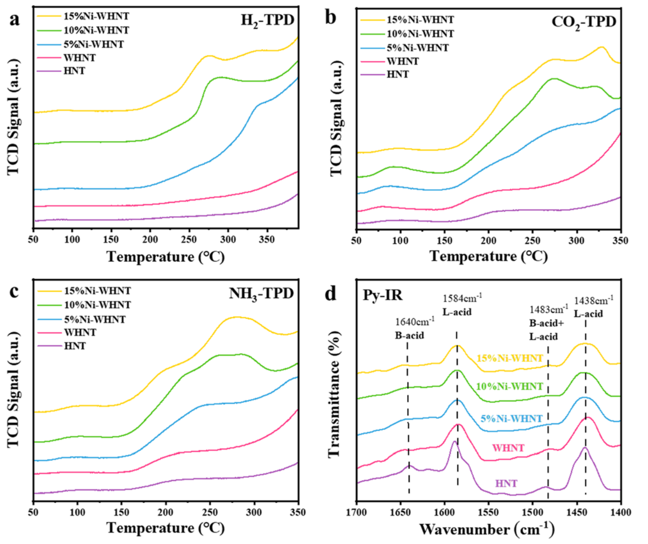

Fig. 8 (a) H_2-TPD curves, (b) CO_2-TPD curves, (c) NH_3-TPD curves, and (d) Py-IR spectra of catalysts.

In order to reveal the surface acidity and basicity of the catalyst, CO_2-TPD, NH_3-TPD, and transform infrared spectra of pyridine adsorption (Py-IR) were performed. From CO_2-TPD (Fig. 8b), it can be found that the HNT itself has certain base sites. After APTES modification, the amount of base sites increased, but there was no significant change after Ni loading. Previous studies have shown that basic supports play a crucial role in increasing the FAM yield and reducing the temperature.[32] Here, the WHNT support precisely enhanced the basicity of the catalyst, which was beneficial for the efficient directional conversion at lower temperatures. According to the analyses of NH_3-TPD (Fig. 8c), HNT itself also had certain acid sites, and as the Ni loading increased, the activated sites gradually shifted towards the low-temperature region.[50] The acid site type (Brønsted/Lewis acid sites) in catalysts was distinguished by Py-IR analysis, as shown in Fig. 8d. The Py-IR spectrum can be divided into four spectral bands at 1438, 1483, 1584, and 1640 cm^{-1}.[51] As reported, the peaks at 1438 and 1584 cm^{-1} are attributed to the interaction between pyridine and Lewis acids.[52–54] The band at 1483 cm^{-1} results from the overlapping of pyridine adsorption on Lewis and Brønsted acid sites. In addition, the band (1640 cm^{-1}) is assigned to the adsorption of pyridine on Brønsted acid sites. Obviously, the introduction of $-NH_2$ by APTES modification results in a weak absorption peak around 1640. Numerous studies have shown that Lewis acid sites are beneficial for promoting the formation of intermediates SIM and PIM in FAL reduction amination.[55] Ni-WHNT retains more Lewis acid sites owing to the presence of abundant Al^{3+} in the HNT support, which can promote the amination. This may be a key factor in achieving efficient directional conversion in this work.

The role of acid–base sites in the FAL conversion reaction was further investigated through shielding experiments on the 10%Ni-WHNT catalyst. Triethylamine and benzoic acid act as acid and base site shields, respectively. Under these conditions of no shielding, triethylamine shielding, and benzoic acid shielding, the FAL conversion rate and FAM yield at 1 h were

View Article Online

Published on 22 December 2025. Downloaded on 4/26/2026 2:36:15 AM.

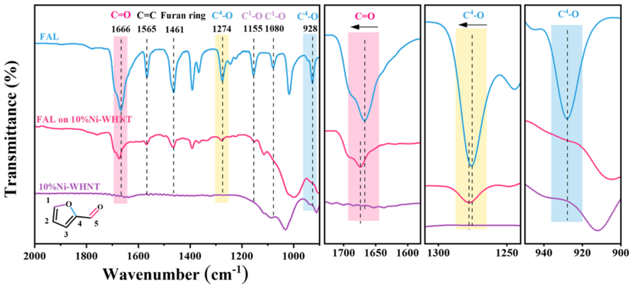

Fig. 9 FT-IR spectra of FAL, 10%Ni-WHNT, and FAL adsorbed on 10% Ni-WHNT.

compared (Fig. S5). Obviously, regardless of the presence of triethylamine or benzoic acid in the catalytic system, the FAM yield is suppressed to near zero. The results indicate that the acid and base are crucial for the titled reaction, confirming the core role of synergistic promotion.

To further investigate the efficient directional conversion of FAL to FAM, adsorption experiments were conducted. As shown in Fig. 9, the absorption peaks of FAL at 1666, 1565, and 1461 cm^{-1} are ascribed to the C–O stretching vibration, C–C antisymmetric stretching vibration, and furan ring breathing vibration, respectively.[56–59] The peaks at 1274 and 928 cm^{-1} correspond to the C^4–O symmetric stretching vibration and in-plane bending vibration, while the peaks at 1155 and 1080 cm^{-1} are attributed to the C^1–O stretching vibration.[60,61] There is a significant difference in the FT-IR spectra of FAL on 10%Ni-WHNT. The peak corresponding to the stretching vibration of C–O shifts towards a higher wavenumber (1673 cm^{-1}), indicating that C–O is adsorbed and activated. Similarly, the peak representing the C^4–O symmetric stretching vibration at 1274 cm^{-1} also shifts to 1279 cm^{-1}, while the characteristic peak at 928 cm^{-1} of C^4–O vibration almost disappears. In sharp contrast, the peak of C–C stretching vibration does not deviate in any way. The above-mentioned results confirm that FAL adsorbs on the catalyst surface in a vertical adsorption manner rather than in a parallel adsorption manner. This adsorption manner is beneficial for the activation of C=O among FAL, which can improve the FAM yield (Fig. S6).[62]

According to the above-mentioned characterizations and analyses, a reasonable catalytic mechanism is clearly understood. FAL is adsorbed on the catalyst surface in a vertical adsorption manner, Ni NPs adsorbs and activates H_2, and Al^{3+} on the support is responsible for the intermediate or NH_3 activation. The acid–base sites of the catalyst can involve in the reaction and thus improve the catalytic performance.

Conclusions

Using the APTES-functionalized HNT as a support, new and efficient Ni-based catalysts were successfully prepared, and they were used to catalyze the reductive amination of biomass FAL for the first time. The APTES modification not only introduced base sites to promote reactions, but also significantly enhanced the metal support interaction, greatly improving the stability and dispersibility of loaded Ni NPs. Under milder reaction conditions (90 °C, 0.5 MPa H_2, 0.3 MPa NH_3), the designed 10%Ni-WHNT catalyst exhibited excellent performance with a FAM yield up to 99%. Besides, it displayed a broad substrate scope and five consecutive-cycle reusability. The interaction between the modified support and nickel facilitated the efficient directional conversion of FAL to FAM. Additionally, the acidity and basicity of catalyst are crucial for the titled reactions. This study utilized the abundant and inexpensive natural mineral (halloysite nanotubes) as a support and non-precious metal nickel as a catalyst to demonstrate a feasible pathway for converting biomass aldehydes into high-value-added chemicals under mild conditions, opening up new possibilities for related fields.

Conflicts of interest

The authors confirm that this article content has no conflict of interest.

Data availability

The authors confirm that the data supporting the findings of this study are available within the article and its supplementary information (SI). Supplementary information is available. See DOI: https://doi.org/10.1039/d5dt02705e.

Acknowledgements

We acknowledge the support from the National Natural Science Foundation of China (22265020 and 22262022) and the Jiangxi Provincial Natural Science Foundation (20252BAC240123).

References

1 K. Murugesan, T. Senthamarai, V. G. Chandrashekhar, *et al.*, Catalytic reductive aminations using molecular hydrogen for synthesis of different kinds of amines, *Chem. Soc. Rev.*, 2020, **49**(17), 6273–6328.
2 Y. Wang, S. Furukawa, X. Fu, *et al.*, Organonitrogen Chemicals from Oxygen-Containing Feedstock over Heterogeneous Catalysts, *ACS Catal.*, 2019, **10**(1), 311–335.
3 M. Pelckmans, T. Renders, S. Van De Vyver, *et al.*, Bio-based amines through sustainable heterogeneous catalysis, *Green Chem.*, 2017, **19**(22), 5303–5331.
4 W. Deng, Y. Wang, S. Zhang, *et al.*, Catalytic amino acid production from biomass-derived intermediates, *Proc. Natl. Acad. Sci. U. S. A.*, 2018, **115**(20), 5093–5098.

This journal is © The Royal Society of Chemistry 2026

Published on 22 December 2025. Downloaded on 4/26/2026 2:36:15 AM.

5 P. Yuan, P. D. Southon, Z. Liu, *et al.*, Functionalization of Halloysite Clay Nanotubes by Grafting with γ-Aminopropyltriethoxysilane, *J. Phys. Chem. C*, 2008, **112**(40), 15742–15751.

6 Y. Li, R. H. Shi, W. W. Lin, *et al.*, A green and recyclable ligand-free copper(I) catalysis system for amination of halonitrobenzenes in aqueous ammonia solution, *Mol. Catal.*, 2019, **475**, 110462.

7 B. C. Feng, B. H. Xi, Z. C. Zhang, *et al.*, Production of Heterocyclic Primary Amines from Heterocyclic Aldehydes on Ni–Mo/ZrO_2, *Chem. Eng. Technol.*, 2022, **45**(6), 1027–1035.

8 Q. Q. Lu, J. G. Liu and L. L. Ma, Recent advances in selective catalytic hydrogenation of nitriles to primary amines, *J. Catal.*, 2021, **404**, 475–492.

9 D. Zhou, L. Zhang, X. Liu, *et al.*, Tuning the coordination environment of single-atom catalyst M–N–C towards selective hydrogenation of functionalized nitroarenes, *Nano Res.*, 2021, **15**(1), 519–527.

10 Y. M. Lin, R. F. Nie, Y. T. Li, *et al.*, Highly efficient and anti-poisoning single-atom cobalt catalyst for selective hydrogenation of nitroarenes, *Nano Res.*, 2022, **15**(12), 10006–10013.

11 G. P. Lu, K. K. Sun, Y. M. Lin, *et al.*, Single-atomic-site iron on N-doped carbon for chemoselective reduction of nitroarenes, *Nano Res.*, 2022, **15**(1), 603–611.

12 B. Feng, R. Guo, Q. Cai, *et al.*, Construction of isolated Ni sites on nitrogen-doped hollow carbon spheres with Ni–N_3 configuration for enhanced reduction of nitroarenes, *Nano Res.*, 2022, **15**(7), 6001–6009.

13 P. J. Chang, H. Y. Cheng and F. Y. Zhao, Photocatalytic Reduction of Aromatic Nitro Compounds with Ag/Ag_xS Composites under Visible Light Irradiation, *J. Phys. Chem. C*, 2021, **125**(47), 26021–26030.

14 T. Senthamarai, K. Murugesan, J. Schneidewind, *et al.*, Simple ruthenium-catalyzed reductive amination enables the synthesis of a broad range of primary amines, *Nat. Commun.*, 2018, **9**(1), 4123.

15 K. Murugesan, Z. Wei, V. G. Chandrashekhar, *et al.*, Homogeneous cobalt-catalyzed reductive amination for synthesis of functionalized primary amines, *Nat. Commun.*, 2019, **10**(1), 5443.

16 B. Wang, Y. Ding, K. Lu, *et al.*, Host-guest chemistry immobilized nickel nanoparticles on zeolites as efficient catalysts for amination of 1-octanol, *J. Catal.*, 2020, **381**, 443–453.

17 Y. D. Du, B. H. Chen and W. Shu, Direct Access to Primary Amines from Alkenes by Selective Metal-Free Hydroamination, *Angew. Chem., Int. Ed.*, 2021, **60**(18), 9875–9880.

18 X. Li, J. Q. Zhao, B. Sun, *et al.*, Preparation of Furanyl Primary Amines from Biobased Furanyl Derivatives over Heterogeneous Catalysts, *ACS Sustainable Chem. Eng.*, 2023, **11**(51), 17951–17978.

19 S. Gomez, J. A. Peters and T. Maschmeyer, The reductive amination of aldehydes and ketones and the hydrogenation of nitriles: Mechanistic aspects and selectivity control, *Adv. Synth. Catal.*, 2002, **344**(10), 1037–1057.

20 T. Komanoya, T. Kinemura, Y. Kita, *et al.*, Electronic Effect of Ruthenium Nanoparticles on Efficient Reductive Amination of Carbonyl Compounds, *J. Am. Chem. Soc.*, 2017, **139**(33), 11493–11499.

21 M. X. Gao, X. Q. Jia, J. P. Ma, *et al.*, Self-regulated catalysis for the selective synthesis of primary amines from carbonyl compounds, *Green Chem.*, 2021, **23**(18), 7115–7121.

22 R. Sun, L. Xiao and W. Wu, *In situ* carbon-encapsulated Ni_2P@C catalysts for reductive amination of furfural, *Mol. Catal.*, 2024, **553**, 113710.

23 M. Manzoli, E. C. Gaudino, G. Cravotto, *et al.*, Microwave-Assisted Reductive Amination with Aqueous Ammonia: Sustainable Pathway Using Recyclable Magnetic Nickel-Based Nanocatalyst, *ACS Sustainable Chem. Eng.*, 2019, **7**(6), 5963–5974.

24 R. Shang, H. Zhang, Y. L. Li, *et al.*, Selective Reductive Amination of 5-Hydroxymethylfurfural under Hypobaric H_2 by a Durable Carbon-Coated Magnetic Ni Catalyst, *ACS Catal.*, 2025, **15**(15), 13322–13336.

25 M. Massaro, R. Noto and S. Riela, Halloysite Nanotubes: Smart Nanomaterials in Catalysis, *Catalysts*, 2022, **12**(2), 149.

26 M. Massaro, C. G. Colletti, G. Lazzara, *et al.*, Halloysite nanotubes as support for metal-based catalysts, *J. Mater. Chem. A*, 2017, **5**(26), 13276–13293.

27 R. Cui, J. Zhou, D. Wang, *et al.*, Double solvent synthesis of ultrafine Pt nanoparticles supported on halloysite nanotubes for chemoselective cinnamaldehyde hydrogenation, *Dalton Trans.*, 2023, **52**(11), 3325–3332.

28 M. Massaro, C. G. Colletti, B. Fiore, *et al.*, Gold nanoparticles stabilized by modified halloysite nanotubes for catalytic applications, *Appl. Organomet. Chem.*, 2018, **33**(3), e4665.

29 L. J. Fu, D. K. Fan, J. Zhang, *et al.*, Microstructure and properties of halloysite nanotubes and modification methods: A comprehensive review, *Appl. Clay Sci.*, 2024, **253**, 107348.

30 Z. X. Gao, L. Y. Cai, H. R. Ma, *et al.*, Dual Scale Hydrogen Transfer Bridge Construction for Biomass Tandem Reductive Amination, *ACS Catal.*, 2023, **13**(19), 12835–12847.

31 X. R. Du, C. S. Gao, J. X. Huang, *et al.*, Efficient Reductive Amination of Furfural to a Primary Amine on a Pt/TiO_2 Catalyst: A Manifestation of the Nanocluster Proximity Effect, *ACS Catal.*, 2025, **15**(6), 4654–4664.

32 M. K. Saini, S. Kumar, H. Li, *et al.*, Advances in the Catalytic Reductive Amination of Furfural to Furfural Amine: The Momentous Role of Active Metal Sites, *ChemSusChem*, 2022, **15**(7), e202200107.

33 A. Philip, J. Lihavainen, M. Keinänen, *et al.*, Gold nanoparticle-decorated halloysite nanotubes – Selective catalysts for benzyl alcohol oxidation, *Appl. Clay Sci.*, 2017, **143**, 80–88.

34 M. L. Zou, M. L. Du, M. Zhang, *et al.*, Synthesis and deposition of ultrafine noble metallic nanoparticles on amino-

Published on 22 December 2025. Downloaded on 4/26/2026 2:36:15 AM.

functionalized halloysite nanotubes and their catalytic application, *Mater. Res. Bull.*, 2015, **61**, 375–382.

35 N. Sahiner and S. B. Sengel, Various amine functionalized halloysite nanotube as efficient metal free catalysts for H_2 generation from sodium borohydride methanolysis, *Appl. Clay Sci.*, 2017, **146**, 517–525.

36 Z. X. Zheng, S. Wang, F. Yang, *et al.*, Controlled surface multifunctional groups over halloysite nanotube enabling reinforced lead adsorption in vitro, *Sep. Purif. Technol.*, 2024, **339**, 126632.

37 H. F. Tian, Z. Y. Chen, X. P. Su, *et al.*, Preparation of Halloysite-Based Hollow Tubular ZSM-5 and Its Catalytic Performance for CO_2 Hydrogenation to p-Xylene, *ACS Sustainable Chem. Eng.*, 2025, **13**(30), 11884–11897.

38 L. Song, K. Tan, Y. Ye, *et al.*, Amine-Functionalized Natural Halloysite Nanotubes Supported Metallic (Pd, Au, Ag) Nanoparticles and Their Catalytic Performance for Dehydrogenation of Formic Acid, *Nanomaterials*, 2022, **12**(14), 2414.

39 Q. Wang, J. P. Zhang and A. Q. Wang, Alkali activation of halloysite for adsorption and release of ofloxacin, *Appl. Surf. Sci.*, 2013, **287**, 54–61.

40 H. Hemmatpour, V. Haddadi-Asl and H. Roghani-Mamaqani, Synthesis of pH-sensitive poly (*N*,*N*-dimethylaminoethyl methacrylate)-grafted halloysite nanotubes for adsorption and controlled release of DPH and DS drugs, *Polymer*, 2015, **65**, 143–153.

41 K. Jeamjumnunja, O. Cheycharoen, N. Phongzitthiganna, *et al.*, Surface-Modified Halloysite Nanotubes as Electrochemical CO_2 Sensors, *ACS Appl. Nano Mater.*, 2021, **4**(4), 3686–3695.

42 Y. Peng, Z. Xu, L. Yu, *et al.*, Trimetallic Cu–Ni–Re/Hβ catalyst for the direct conversion of furfural to 2-Methyltetrahydrofuran, *Chem. Eng. J.*, 2023, **454**, 139746.

43 Y. Li, B. Liu, Y. Wang, *et al.*, High-Performance Ni_3P Catalyst for C═O Hydrogenation of Ethyl Levulinate: $Ni^{\delta+}$ as Outstanding Adsorption Sites, *ACS Catal.*, 2022, **12**(13), 7926–7935.

44 Y. S. Zhang, R. F. Nie, A. Rezayan, *et al.*, On-Demand, Highly Tunable, and Selective 5-Hydroxymethylfurfural Hydrogenation to Furan Diols Enabled by Ni and Ni_3Ga Alloy Catalysts, *ACS Catal.*, 2023, **13**(1), 803–814.

45 W. Lin, Y. Zhang, Z. Ma, *et al.*, Synergy between Ni_3Sn_2 alloy and Lewis acidic ReO_x enables selectivity control of furfural hydrogenation to cyclopentanone, *Appl. Catal., B*, 2024, **340**, 123191.

46 T. Bao, Y. Wu, C. Tang, *et al.*, Highly Ordered Conductive Metal–Organic Frameworks with Chemically Confined Polyoxometalate Clusters: A Dual-Functional Electrocatalyst for Efficient H_2O_2 Synthesis and Biomass Valorization, *Adv. Mater.*, 2025, **37**(17), e2500399.

47 Z. H. Zhang, R. Z. Liu, L. Huang, *et al.*, Highly efficient selective hydrogenation of furfural to tetrahydrofurfuryl alcohol over MOF-derived Co–Ni bimetallic catalysts: The effects of Co–Ni alloy and adsorption configuration, *J. Catal.*, 2024, **440**, 115824.

48 Z. H. Zhang, R. Z. Liu, L. Huang, *et al.*, Understanding the reaction route of selectively converting furfural to furan over the alkali-induced Co–Mo_2C heterostructure, *Chem. Eng. J.*, 2023, **466**, 143237.

49 Y. Yang, L. Zhou, X. Wang, *et al.*, Catalytic reductive amination of furfural to furfurylamine on robust ultra-small Ni nanoparticles, *Nano Res.*, 2023, **16**(3), 3719–3729.

50 G. Zasypalov, A. Vutolkina, V. Klimovsky, *et al.*, Hydrodeoxygenation of guaiacol over halloysite nanotubes decorated with Ru nanoparticles: Effect of alumina acid etching on catalytic behavior and reaction pathways, *Appl. Catal., B*, 2024, **342**, 123425.

51 W. Luo, K. Liu, T. Luo, *et al.*, Promoting C–F Bond Activation for Perfluorinated Compounds Decomposition via Atomically Synergistic Lewis and Bronsted Acid Sites, *J. Am. Chem. Soc.*, 2025, **147**(9), 7391–7399.

52 X. Weng, P. Sun, Y. Long, *et al.*, Catalytic Oxidation of Chlorobenzene over $Mn_xCe_{1(x}O_2$/HZSM-5 Catalysts: A Study with Practical Implications, *Environ. Sci. Technol.*, 2017, **51**(14), 8057–8066.

53 L. Xing, K. Wei, Q. Li, *et al.*, One-Step Synthesized SO_4^{2-}/ZrO^{2-}HZSM-5 Solid Acid Catalyst for Carbamate Decomposition in CO_2 Capture, *Environ. Sci. Technol.*, 2020, **54**(21), 13944–13952.

54 J. Guo, S. Zhu, Y. Cen, *et al.*, Ordered mesoporous Nb–W oxides for the conversion of glucose to fructose, mannose and 5-hydroxymethylfurfural, *Appl. Catal., B*, 2017, **200**, 611–619.

55 Z. Wang, Y. Zheng, J. Feng, *et al.*, Promoting Amination of Furfural to Furfurylamine by Metal-Support Interactions on Pd/MoO_{3-x} Catalysts, *Chem. Eur. J.*, 2023, **29**(47), e202300947.

56 W. Liu, Y. Yang, L. Chen, *et al.*, Atomically-ordered active sites in NiMo intermetallic compound toward low-pressure hydrodeoxygenation of furfural, *Appl. Catal., B*, 2021, **282**, 119557.

57 Q. Wang, J. Feng, L. Zheng, *et al.*, Interfacial Structure-Determined Reaction Pathway and Selectivity for 5-(Hydroxymethyl) furfural Hydrogenation over Cu-Based Catalysts, *ACS Catal.*, 2019, **10**(2), 1353–1365.

58 T. Xiao, X. Liu, G. Xu, *et al.*, Phase tuning of ZrO_2 supported cobalt catalysts for hydrodeoxygenation of 5-hydroxymethylfurfural to 2,5-dimethylfuran under mild conditions, *Appl. Catal., B*, 2021, **295**, 120270.

59 Y. Zhu, W. Zhao, J. Zhang, *et al.*, Selective Activation of C–OH, C–O–C, or C═C in Furfuryl Alcohol by Engineered Pt Sites Supported on Layered Double Oxides, *ACS Catal.*, 2020, **10**(15), 8032–8041.

60 M. Rogojerov, G. Keresztury and B. Jordanov, Vibrational spectra of partially oriented molecules having two conformers in nematic and isotropic solutions: furfural and 2-chlorobenzaldehyde, *Spectrochim. Acta, Part A*, 2005, **61**(7), 1661–1670.

61 Z. K. Tong, X. Li, J. Y. Dong, *et al.*, Adsorption Configuration-Determined Selective Hydrogenative Ring

This journal is © The Royal Society of Chemistry 2026

Published on 22 December 2025. Downloaded on 4/26/2026 2:36:15 AM.

Opening and Ring Rearrangement of Furfural over Metal Phosphate, *ACS Catal.*, 2021, **11**(11), 6406–6415.

62 Y. Li, Q. Shen, Y. Nian, *et al.*, Promoting effect of oxygen vacancies in Co/CoAl_2O_4 catalyst steered with a straightforward method on hydrogenation of furfural to 2-methylfuran, *Appl. Catal., B*, 2024, **343**, 123539.

63 H. Qi, J. Yang, F. Liu, *et al.*, Highly selective and robust single-atom catalyst Ru_1/NC for reductive amination of aldehydes/ketones, *Nat. Commun.*, 2021, **12**(1), 3295.

64 C. Xie, J. L. Song, M. L. Hua, *et al.*, Ambient-temperature synthesis of primary amines via reductive amination of carbonyl compounds, *ACS Catal.*, 2020, **10**(14), 7763–7772.

65 B. Dong, X. C. Guo, B. Zhang, *et al.*, Heterogeneous Ru-based catalysts for one-pot synthesis of primary amines from aldehydes and ammonia, *Catalysts*, 2015, **5**(4), 2258–2270.

66 W. J. Guo, Z. Q. Wang, S. Xiang, *et al.*, Co@CoO-catalyzed reductive amination driven by hydride-like ${NH_2}^{\delta-}$ species, *Chin. J. Catal.*, 2023, **47**, 181–190.

67 B. X. Zheng, J. Xu, J. J. Song, *et al.*, Nanoparticles and single atoms of cobalt synergistically enabled low-temperature reductive amination of carbonyl compounds, *Chem. Sci.*, 2022, **13**(31), 9047–9055.

68 Z. Ma, C. Kuloor, C. Kreyenschulte, *et al.*, Development of iron-based single atom materials for general and efficient synthesis of amines, *Angew. Chem., Int. Ed.*, 2024, **63**(37), e202407859.

69 W. J. Song, Y. J. Wan, Y. F. Li, *et al.*, Electronic Ni–N interaction enhanced reductive amination on an N-doped porous carbon supported Ni catalyst, *Catal. Sci. Technol.*, 2022, **12**(23), 7208–7218.

70 Y. J. Wan, P. F. Ma, H. L. Lu, *et al.*, External [1 1 1] facets on nanorod gamma alumina boosts catalytic reductive amination of carbonyl compound to primary amine, *J. Catal.*, 2024, **429**, 115–125.

71 Y. Yang, L. Zhou, X. Wang, *et al.*, Catalytic reductive amination of furfural to furfurylamine on robust ultra-small Ni nanoparticles, *Nano Res.*, 2023, **16**(3), 3719–3729.

72 Y. M. Zhang, H. M. Yang, Q. Chi, *et al.*, Nitrogen-Doped Carbon-Supported Nickel Nanoparticles: A Robust Catalyst to Bridge the Hydrogenation of Nitriles and the Reductive Amination of Carbonyl Compounds for the Synthesis of Primary Amines, *ChemSusChem*, 2019, **12**(6), 1246–1255.

73 C. L. Dong, Y. S. Wang, H. T. Peng, *et al.*, Facile and Efficient Synthesis of Primary Amines via Reductive Amination over a Ni/Al_2O_3 Catalyst, *ACS Sustainable Chem. Eng.*, 2021, **9**(21), 7318–7327.

74 Z. Y. Pan, Q. Zhang, W. Q. Wang, *et al.*, Size-Tunable Carbon-Doped Ni Nanoparticles for Switchable Reductive Amination of Biomass-Derived Carbonyl Compounds to Primary Amines and Secondary Imines, *ACS Sustainable Chem. Eng.*, 2022, **10**(11), 3777–3786.

75 H. J. Wang, Y. C. Zhang, D. Luo, *et al.*, Active Metal Dependent Side Reactions for the Reductive Amination of Furfural, *Mol. Catal.*, 2023, **536**, 112914.